

See discussions, stats, and author profiles for this publication at: <https://www.researchgate.net/publication/278741767>

# Anticorrosive Oligoaniline-Contained Electroactive Siliceous Hybrid Materials

ARTICLE *in* RSC ADVANCES · JUNE 2015

Impact Factor: 3.84 · DOI: 10.1039/C5RA08591H

CITATIONS

2

READS

34

## 4 AUTHORS, INCLUDING:



**Lin Gu**

Chinese Academy of Sciences

**14** PUBLICATIONS **70** CITATIONS

SEE PROFILE



**Shuan Liu**

Ningbo Institute of Materials Technology a...

**21** PUBLICATIONS **82** CITATIONS

SEE PROFILE



**Haibin Yu**

Chinese Academy of Sciences, Ningbo

**10** PUBLICATIONS **88** CITATIONS

SEE PROFILE

CrossMark  
click for updatesCite this: *RSC Adv.*, 2015, 5, 56011

# Anticorrosive oligoaniline-containing electroactive siliceous hybrid materials

Lin Gu, Shuan Liu,\* Haichao Zhao\* and Haibin Yu

In this work, a novel electroactive silsesquioxane precursor, *N*-(3-triethoxysilylpropylureido) aniline tetramer (TESPAT), was synthesized *via* one-step coupling reaction between phenyl-capped aniline tetramer (AT) and 3-(triethoxysilyl)propyl isocyanate (TESPIC) under mild conditions. The chemical structure and electroactivity of the resulting silsesquioxane precursor were investigated by FTIR, NMR, UV-vis spectra, and cyclic voltammetry. Subsequently, the sol-gel reactions of TESPAT with triethoxymethylsilane (TEMS) at various compositions were carried out to achieve new electroactive siliceous hybrid materials with good thermal stability. Furthermore, polarization curves and electrochemical impedance spectroscopic (EIS) measurements indicated that the obtained hybrid materials exhibit remarkably enhanced corrosion protection on Q235 electrodes as compared to pure silica coating. The significantly improved anticorrosion performance is attributed to the redox catalytic capabilities of the AT units in the hybrid materials.

Received 8th May 2015  
Accepted 17th June 2015

DOI: 10.1039/c5ra08591h

www.rsc.org/advances

## 1. Introduction

Silica-based organic-inorganic hybrid materials have attracted a great deal of attention during the last decade since they combine the advantages of organic and inorganic components, and have found numerous applications in many fields such as optical devices,<sup>1</sup> chemical and biological sensors,<sup>2</sup> catalysts,<sup>3</sup> biofouling<sup>4</sup> and corrosion protection.<sup>5</sup> It is noteworthy that the versatility of sol-gel processes enables a wide range of organically-modified silica-based hybrid materials to be made under mild conditions.<sup>6</sup> Incorporating organic components into inorganic silica offers extensive possibilities to tune the structure and properties of the final materials.<sup>7</sup> As far as corrosion protection is concerned, organic inhibitors have also been introduced into the sol-gel system, therefore, providing different mechanism of corrosion protection for metallic substrates without using toxic heavy metals.<sup>7,8</sup> However, to the best of our knowledge, there are still few reports on the incorporation of electroactive polymers as corrosion inhibitors into inorganic silica materials for advanced anticorrosive coatings.<sup>9,10</sup>

Intrinsically conducting polymers, such as polyaniline (PAN), polypyrrole, and polythiophene, have emerged as attractive materials due to their potentially commercial applications in electrode materials,<sup>11,12</sup> photo-electronic devices,<sup>13</sup> and sensors,<sup>14</sup> *etc.* Among these electroactive polymers, PAN has been known to be one of the most promising materials in anticorrosion coatings as an alternative to chromium-containing systems because

of its environmental stability, chemical redox reversibility, and relatively low cost.<sup>9,15–18</sup> More interestingly, it has been reported that PAN coatings can protect metal even at coating defect.<sup>18</sup> However, the poor solubility of PAN in many organic solvents has limited its practical applications. Compared with PAN, oligoaniline exhibits excellent solubility and well-defined molecular structures.<sup>19,20</sup> Moreover, the electroactivity of aniline oligomer is remarkably similar to that of PAN.<sup>21–23</sup> Therefore, aniline oligomer offers the opportunities to design and produce well-defined species with anticorrosive performance.

Our study aims to covalently incorporate electroactive organic species as corrosion inhibitors into inorganic silica for advanced anticorrosive coatings. In this paper, a novel aniline tetramer-siliceous precursor, *N*-(3-triethoxysilylpropylureido) aniline tetramer (TESPAT) was successfully synthesized for the first time *via* one-step coupling reaction between phenyl-capped aniline tetramer (AT) and 3-(triethoxysilyl)propyl isocyanate (TESPIC). The new aniline tetramer-siliceous compound was extensively characterized by FTIR, NMR, UV-vis spectra, and cyclic voltammetry. Subsequently, new electroactive siliceous hybrid materials have also been prepared through the sol-gel reactions of TESPAT with triethoxymethylsilane (TEMS) at various compositions. The hybrid materials exhibit remarkably enhanced corrosion protection as compared to pure silica coating, based on a series of electrochemical measurements performed under a saline condition.

## 2. Experimental

### 2.1 Materials

3-(Triethoxysilyl)propyl isocyanate (TESPIC), anhydrous tetrahydrofuran (THF), 4-amino diphenylamine and triethoxymethylsilane

Key Laboratory of Marine Materials and Related Technologies, Zhejiang Key Laboratory of Marine Materials and Protective Technologies, Ningbo Institute of Materials Technology and Engineering, Chinese Academy of Sciences, Ningbo 315201, P. R. China. E-mail: liushuan@nimte.ac.cn; zhaohaichao@nimte.ac.cn; Tel: +86 0574 87911126

(TEMS) were purchased from Aladdin Industrial Corporation, and were used without further purification. Concentrated HCl, acetone, ammonium hydroxide and petroleum ether are analytically pure, and were used as received. The Q235 steel was polished with 800 and 1500 sand paper, and then degreased by ultrasonication in acetone.

## 2.2 Synthesis of aniline tetramer (AT)

The aniline tetramer was prepared according to the literature.<sup>24</sup> In brief, 4-amino diphenylamine (7.36 g, 40 mmol) was dissolved in a mixture of acetone (200 mL), concentrated HCl (50 mL) and water (200 mL) at 0 °C in an ice bath. Ammonium persulfate (9.13 g, 40 mmol) in acetone/water (50 mL/50 mL) solution was then added dropwise into the above solution during 1 h with vigorous stirring. The reaction was carried out in air for 4 h. The mixture was filtered to collect the AT, the cake was then washed with 200 mL of 0.1 M HCl and 100 mL of water. The AT was dedoped in 200 mL of 1 M NH<sub>4</sub>OH for 4 h, and was filtered and washed with water until the filtrate was neutral. Finally, the AT was dried at 60 °C in vacuum for 48 h. Yield: ~95%.

## 2.3 Synthesis of *N*-(3-triethoxysilylpropylureido) aniline tetramer (TESPAT)

Aniline tetramer (3 g, 8.18 mmol) was added into a three-neck round flask contained anhydrous THF (40 mL) and 3-(triethoxysilyl)propyl isocyanate (TESPIC, 2.4 g, 9.7 mmol) under magnetic stirring before refluxing for 24 h under N<sub>2</sub> atmosphere. After the reaction was cooled down to room temperature, 200 mL of petroleum ether was added dropwise into the solution. The black solid was collected by filtration. Further purification was achieved by reprecipitation from THF/petroleum ether, and then dried at 60 °C in vacuum till constant weight. Yield: ~98%.

## 2.4 Preparation of tetramer-containing sol-gel solution and coating deposition

A convenient sol-gel approach was used to prepare novel electroactive aniline tetramer-containing hybrid materials. Typically, TEMS (1.78 g, 0.01 mol) was added to a mixture of 0.01 mol L<sup>-1</sup> formic acid solution (2 g) and ethanol (3.2 g) with continuous stirring for 1 h to obtain a clear solution (sol A). Meanwhile, 2 g (3.2 mmol) of TESPAT were dissolved in 98 g of ethanol. After bath-sonication for 10 min, a homogeneous solution (sol B) was formed. Sol B was then mixed with sol A at various weight ratios (referred as 2 wt%, 5 wt% and 10 wt%) according to the wt% of TESPAT in the content of TEMS. The mixed sols were kept stirring at room temperature for 24 h.

Q235 steel electrodes were immersed into the above mixed sols for 2 min at room temperature and dried at 100 °C for 1 h in an air oven.

## 2.5 Characterizations

<sup>1</sup>H NMR spectra were recorded at room temperature on a NMR spectrometer (400 MHz AVANCE III, Bruker) in deuterated

dimethyl sulfoxide (DMSO-*d*<sub>6</sub>). FTIR spectra were performed on a spectrometer (NICOLET 6700, Thermo) by collecting 32 scans at a spectral resolution of 4 cm<sup>-1</sup>. UV-vis spectra were obtained using a UV-vis spectrometer (Lambda 950, Perkin-Elmer). Thermo gravimetry analysis (TGA) was tested on a Perkin-Elmer Pyris Diamond thermal analyzer under a N<sub>2</sub> atmosphere at a heating rate of 20 °C min<sup>-1</sup> from 30 °C to 500 °C.

Electrochemical impedance spectroscopy (EIS) was performed on a CHI-660E electrochemical system in 3.5 wt% NaCl aqueous solution. A classical three-electrode cell system was employed, consisting of a coating/Q235 steel as the working electrode, a saturated calomel electrode (SCE) equipped with a Luggin capillary as the reference electrode and a platinum plate of 2.5 cm<sup>2</sup> as the counter electrode. For EIS, the test frequency range was 10<sup>-5</sup>–10<sup>-2</sup> Hz and the amplitude of the sinusoidal voltage signal was 20–50 mV. EIS data were analyzed by ZsimpWin 3.21 software. Polarization curves were recorded from -200 mV to +200 mV *versus* open circuit potential (OCP) by changing the electrode potential automatically with a scan rate of 0.5 mV s<sup>-1</sup>. Cyclic voltammetry (CV) measurements were carried out in aqueous HCl solution (1 M). A glass carbon electrode was used as the working electrode. The scan rate was 20 mV s<sup>-1</sup>.

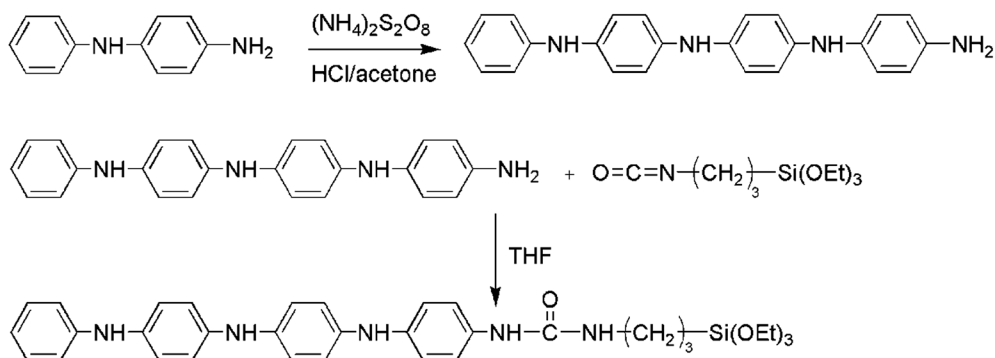
# 3. Results and discussion

## 3.1 Synthesis and characterization of TESPAT

**3.1.1 Synthesis and structure analysis of TESPAT.** *N*-(3-Triethoxysilylpropylureido) aniline tetramer (TESPAT) was synthesized based on the reaction between the amino groups of AT and the isocyanate groups of TESPIC, as shown in Scheme 1.

The obtained TESPAT was characterized by FTIR, <sup>1</sup>H NMR and UV-vis spectra. Fig. 1 shows FTIR spectra of the AT and TESPAT. The sharp absorption peaks at 3024, 1596, and 1504 cm<sup>-1</sup> are assigned to stretching vibrations of the phenyl C–H, quinoid and benzenoid ring, respectively. The peaks at 1301 and 1221 cm<sup>-1</sup> belong to stretching vibrations of the C–N groups. As can be seen from curve b, the new sharp absorption peaks at *ca.* 2900 cm<sup>-1</sup> are attributed to the presence of aliphatic sp<sup>3</sup> C–H stretching vibrations, while sharp absorption peaks at 1641 and 1166 cm<sup>-1</sup> are ascribed to stretching vibrations of C=O in the ureido unit (–NH–CO–NH–) and C–O in –OCH<sub>2</sub>CH<sub>3</sub> group, respectively, indicating that a reaction has occurred between the amino groups of AT with the isocyanate groups of TESPIC.

Fig. 2 shows <sup>1</sup>H NMR spectra of the AT and TESPAT. The signals assigned to the –NH<sub>2</sub> and –NH groups of AT are present at 5.5 and 8.3 ppm, respectively (Fig. 2a). However, the signal at 5.5 ppm has totally disappeared in Fig. 2b for TESPAT, which further demonstrated the occurrence of the reaction between –NH<sub>2</sub> groups of AT and the isocyanate groups of TESPIC. The –NH group signal at 8.3 ppm still exists after the reaction of TESPIC with AT, suggesting that the coupling reaction only took place at the end group of aniline tetramer (AT). Furthermore, the new peaks at 3.0, 1.5 and 0.5 ppm are assigned to the CH<sub>2</sub> groups between the ureido unit and siloxy group (–Si(OEt)<sub>3</sub>),



Scheme 1 Synthesis of *N*-(3-(triethoxysilyl)propylureido) aniline tetramer (TESPAT).

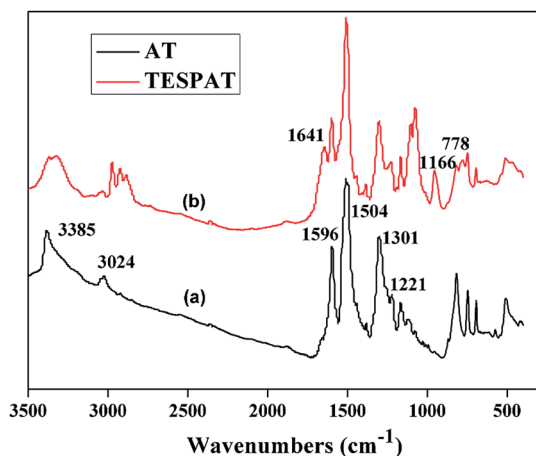


Fig. 1 FTIR spectra of AT (a) and TESPAT (b).

while the signals at 3.7 and 1.1 ppm are ascribed to the  $\text{CH}_2$  and  $\text{CH}_3$  groups in  $-\text{OCH}_2\text{CH}_3$  unit, respectively.

Fig. 3 shows UV-vis spectra of the AT and TESPAT in ethanol. The pure TA shows two distinct absorption peaks at 314 and 594 nm (curve a), which are assigned to the  $\pi-\pi^*$  transition of the benzene ring and the benzenoid (B) to quinoid (Q)  $\pi_{\text{B}}-\pi_{\text{Q}}$

excitonic transition.<sup>25–27</sup> Similar to AT, the TESPAT exhibit two distinct absorption peaks at 311 and 587 nm (curve b). However, the Q/B intensity ratio of TESPAT decreased along with a slight blue shift, which may be ascribed to enhanced resonance from the formation of ureido moiety that facilitates the delocalization of electrons in benzene units.<sup>28</sup> This also confirmed that a coupling reaction had occurred between AT and TESPIC.

**3.1.2 Electrochemical characterization of TESPAT.** As is well known, oligoanilines similar to polyanilines have different oxidation states (that is, leucoemeraldine base (LEB), emeraldine base (EB), and pernigraniline base (PB)) when they are treated by oxidizing and reducing agents or upon on different voltages.<sup>29</sup> The electrochemical properties of the as-prepared TESPAT were investigated by cyclic voltammetry (CV), as is shown in Fig. 4. There are two pairs of well-defined oxidation peaks at 0.341 and 0.490 V, which can be assigned to the transition from a LEB form to an EB form and a further transition to a PB form, respectively (Scheme 2).<sup>27,30</sup> This result demonstrated that the as-prepared TESPAT has good electroactivity.

### 3.2 Anticorrosive electroactive aniline tetramer-containing hybrid materials through sol-gel process

**3.2.1 Structural and electrochemical characterization of hybrid materials.** A novel electroactive aniline tetramer-containing hybrid material was obtained by the sol-gel

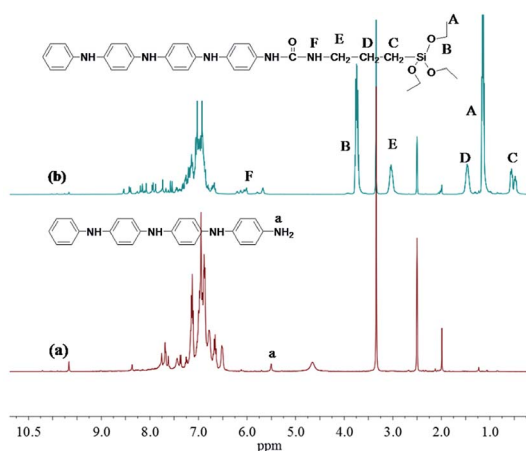


Fig. 2  $^1\text{H}$  NMR spectra of AT (a) and TESPAT (b).

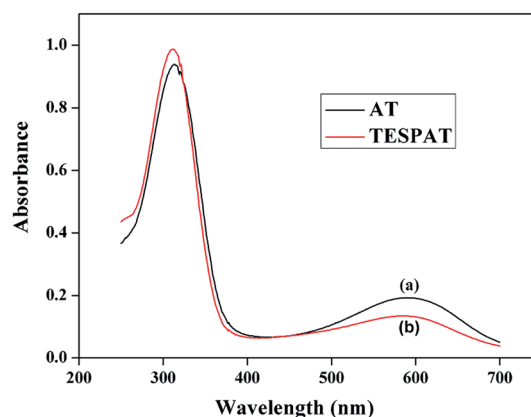


Fig. 3 UV-vis spectra of AT (a) and TESPAT (b). Solvent: ethanol.

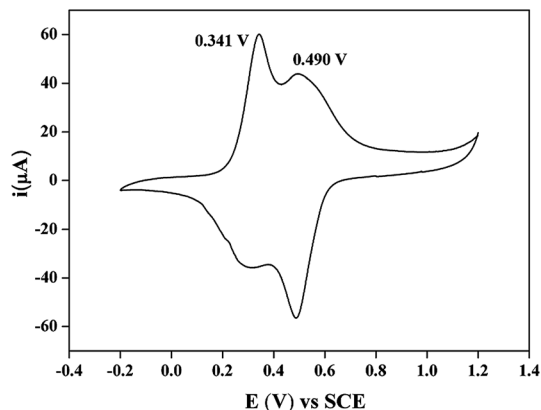
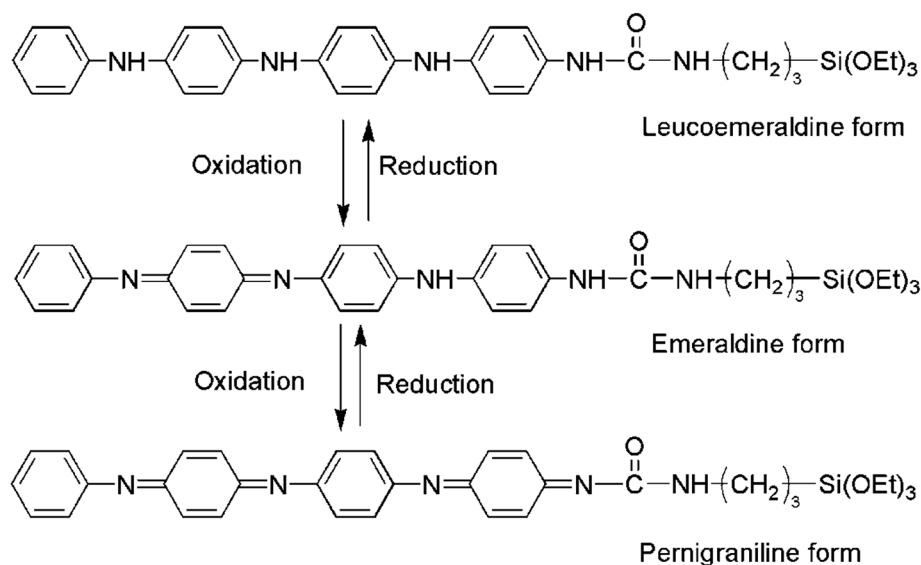


Fig. 4 Cyclic voltammogram of TESPAT in 1 M HCl solution.

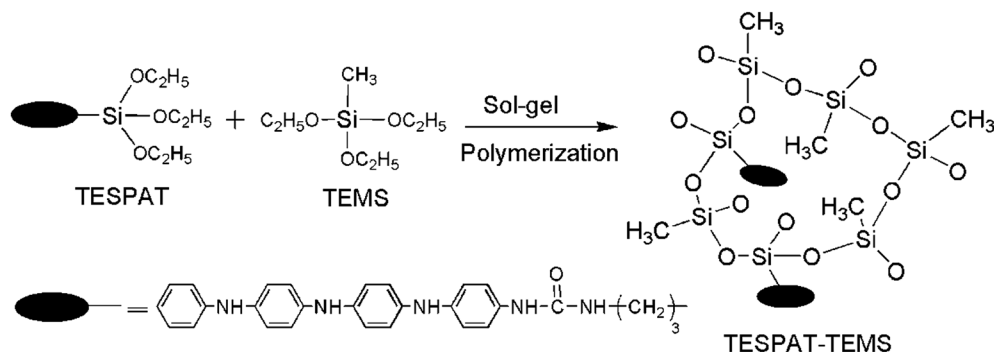
reaction of TESPAT with TEMS, as shown in Scheme 3. The molecular structure of the obtained hybrid materials was confirmed by FTIR spectra, as shown in Fig. 5. For TEMS, the strong absorption peaks at 1113, 1058, and 958  $\text{cm}^{-1}$  are assigned to the asymmetrical stretching vibrations of

$\text{Si-OC}_2\text{H}_5$ .<sup>31</sup> As discussed above (Fig. 1b), the sharp peak appears at 1166  $\text{cm}^{-1}$  ascribed to stretching vibrations of C–O in  $\text{Si-OC}_2\text{H}_5$  group of TESPAT. However, these peaks have disappeared and a new absorbance of Si–OH at 915  $\text{cm}^{-1}$  appears after sol-gel process (Fig. 5b and c), indicating that the hydrolysis reaction occurred. Furthermore, the new strong absorbance bands around 1121 and 1031  $\text{cm}^{-1}$  demonstrated that the hybrid materials have formed the Si–O–Si network (Fig. 5c). In addition, the hybrid materials have good thermal stability due to the formation of the Si–O–Si network (Fig. 6). The morphology of the hybrid material coating was displayed in SEM images as shown in Fig. 7. The pure silica showed a rough surface with many microcracks, while the hybrid material exhibited a relatively smooth surface, which is possibly due to the incorporation of organic content making the coating more flexible.

The electroactivity of the resulting hybrid materials was investigated by CV, as can be seen in Fig. 8. Only one well-defined oxidation/reduction peak at 0.516 V was observed for the hybrid material in HCl aqueous solution, which could be ascribed to the transition from a LEB form to an EB form. This



Scheme 2 Molecular structure of TESPAT in various oxidation states.



Scheme 3 Preparation of aniline tetramer-containing hybrid materials through sol-gel process.

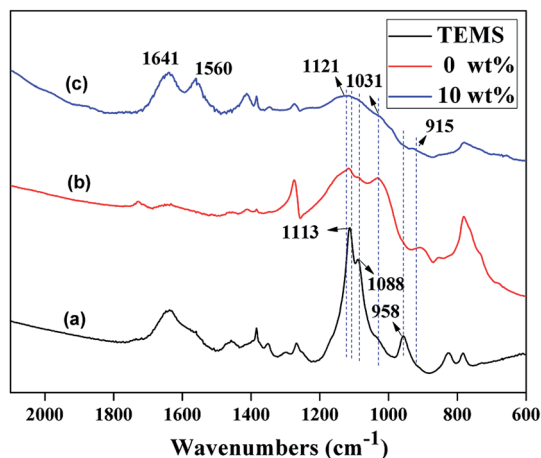


Fig. 5 FTIR spectra of TEMS (a), TESPAT (b) and 10 wt% TEMS–TESPAT (c).

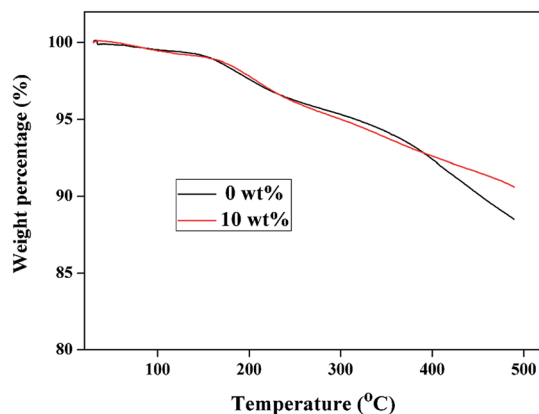


Fig. 6 TGA of hybrid materials from TESPAT–TEMS at different percentage of TESPAT.

result is in agreement with the electrochemical property of poly(methacrylamide) containing aniline tetramer side chains.<sup>32</sup> Therefore, the AT segments in the hybrid materials maintain their electroactivity.

PAN had been previously reported as an advanced anticorrosive coating material due to its redox catalytic properties of conjugated structures that induced the formation of a passive layer of metal oxide, resulting in effective protection against

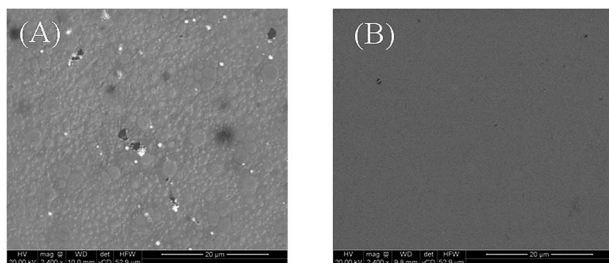


Fig. 7 SEM images of pure silica (A) and hybrid material from TESPAT–TEMS at 5 wt% TESPAT (B).

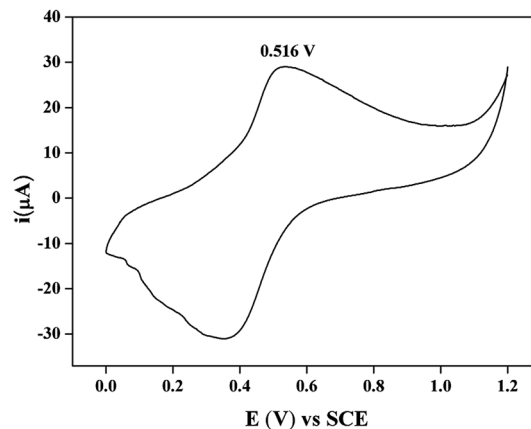


Fig. 8 Cyclic voltammogram of hybrid materials from TESPAT–TEMS with 10 wt% TESPAT in 1 M HCl solution.

corrosion on various metallic surfaces.<sup>22,23,33,34</sup> Therefore, it is conceivable that the redox behavior of the as-prepared hybrid materials would probably display an enhanced anticorrosive performance similar to that of PAN, as discussed in the following sections.

**3.2.2 Anticorrosion behaviors of hybrid materials.** A series of electrochemical measurements were used to investigate the anticorrosion behaviors of the hybrid materials. Fig. 9 shows the Tafel polarization curves of bare, pure silica-coated and hybrid material-coated Q235 steel after immersion in 3.5% NaCl for 24 h. The cathodic and anodic branches of the polarization curves displayed a typical Tafel behavior. Generally, Tafel regions are identified and corrosion parameters are determined by superimposing a straight line along the linear portion of the cathodic and anodic curve and extrapolating it to corrosion potential ( $E_{\text{corr}}$ ). Therefore, the corrosion current density ( $i_{\text{corr}}$ ), corrosion potential ( $E_{\text{corr}}$ ), anodic and cathodic Tafel slopes ( $b_a$ ,  $b_c$ ) were determined from the extrapolation of the Tafel zone of the cathodic and anodic branches and then summarized in Table 1.

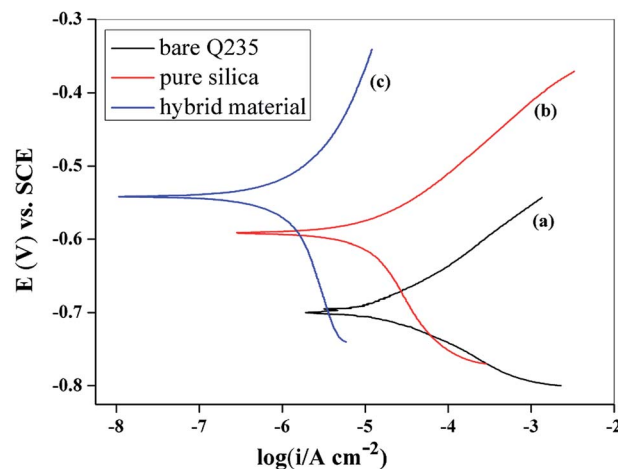


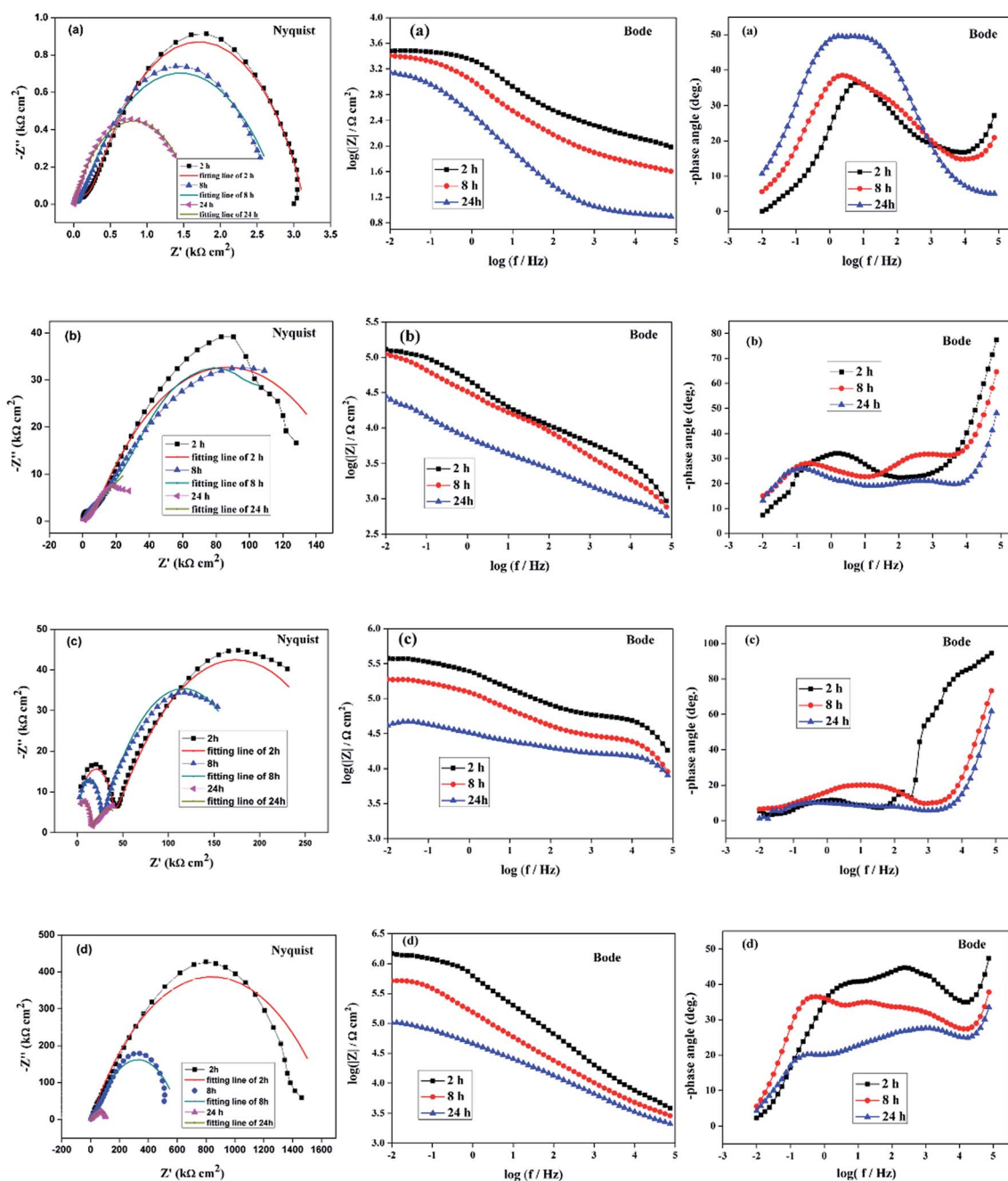
Fig. 9 The polarization curves of bare (a), pure silica-coated (b) and hybrid material-coated (c) Q235 steel electrodes after immersion in 3.5% NaCl for 24 h.



**Table 1** Corrosion parameters of bare, pure silica-coated and hybrid material-coated Q235 steel electrodes after immersion in 3.5% NaCl for 24 h

	$E_{\text{corr}}$ V, vs. SCE	$i_{\text{corr}}$ $\mu\text{A cm}^{-2}$	$b_a$ mV dec $^{-1}$	$b_c$ mV dec $^{-1}$	$R_p$ K $\Omega$ cm $^2$	Thickness $\mu\text{m}$	$P_{\text{EF}}$ (%)
Bare <sup>a</sup>	−0.693	17.1	72.8	60.2	0.83	—	—
Pure silica <sup>b</sup>	−0.592	10.5	85.9	214.2	2.53	2	38.6
Hybrid material <sup>c</sup>	−0.557	1.32	212.8	333.4	42.73	2	92.3
Hybrid material <sup>d</sup>	−0.646	3.89	94.5	234.6	7.84	2	77.2

<sup>a</sup> Bare Q235 steel. <sup>b</sup> Pure silica from TEMS. <sup>c</sup> Hybrid material from TESPAT-TEMS at 5 wt% TESPAT. <sup>d</sup> Hybrid material from TESPAT-TEMS at 10 wt% TESPAT.

**Fig. 10** The Nyquist and Bode plots of pure silica from TEMS (a) and the hybrid materials from TESPAT-TEMS at different percentage of TESPAT: (b) 2 wt%; (c) 5 wt%; (d) 10 wt% immersed in 3.5% NaCl solution as a function of time.

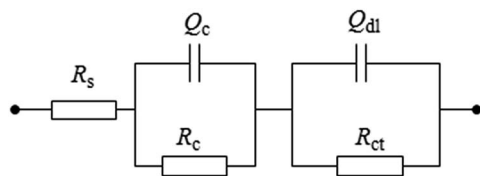


Fig. 11 The equivalent circuit used to fit the EIS data.

The protection efficiency values were calculated using the following equation:<sup>23</sup>

$$P_{\text{EF}}\% = \frac{i_{\text{corr}}(\text{uncoated}) - i_{\text{corr}}(\text{coated})}{i_{\text{corr}}(\text{uncoated})} \times 100\%$$

Tafel plot of the hybrid material-coated Q235 electrode gave a corrosion potential of  $E_{\text{corr}} = -0.557$  V, which was found to be more positive than pure silica-coated ( $-0.592$  V) and bare Q235 steel ( $-0.693$  V). The shift of the  $E_{\text{corr}}$  is probably due to the oxide formation induced by the EB-to-LEB transition.<sup>35</sup> Furthermore, the  $i_{\text{corr}}$  value of the Q235 electrode coated with the hybrid material ( $1.32 \mu\text{A cm}^{-2}$ ) was much lower than that of pure silica-coated ( $10.1 \mu\text{A cm}^{-2}$ ) and bare Q235 steel ( $17.1 \mu\text{A cm}^{-2}$ ), which was only one tenth of the bare Q235 steel. Moreover, the absolute values of  $b_a$  and  $b_c$  of hybrid material were found to be larger than those of bare Q235 carbon steel, suggesting that both of the cathodic and anodic reaction were inhibited in the Q235 electrode coated with the hybrid material. It was noted that the  $P_{\text{EF}}\%$  of the hybrid material (92.3%) was much higher than that of pure silica (38.6%). When the metal is step by step oxidized into metal oxide forming dense oxide barrier for corrosive ions penetration, PAN (or oligoaniline) itself is reduced to lower oxidation state since the electrochemical potential of PAN is much higher than that of Fe.<sup>36</sup> Moreover, PAN can be oxidized to its original oxidation state by the oxygen in the air, and a new run of redox reaction can start.<sup>36</sup> Therefore, the enhanced anticorrosive performance of the hybrid material coated on Q235 steel may result from the redox catalytic capabilities of the AT units in the hybrid material, then forming passive metal oxide layers on the iron surface.<sup>19,37,38</sup>

EIS was further explored to evaluate the degradation processes of various samples immersed in 3.5% NaCl solution as a function of time, as shown in Fig. 10. The impedance modulus at low frequency (such as  $|Z|_{0.01 \text{ Hz}}$ ) represents the ability of the coating to impede the flow of current between anodic and cathodic areas, which is inversely proportional to corrosion rate.<sup>39</sup> The  $|Z|_{0.01 \text{ Hz}}$  value of the hybrid material-coated Q235 electrode was  $101.5 \text{ K}\Omega \text{ cm}^2$  after 24 h immersion (Fig. 9d), which was much higher than that of pure silica-coated ( $1.4 \text{ K}\Omega \text{ cm}^2$ ) (Fig. 9a).

It can be seen that all the EIS exhibited a capacitive arc at the high frequency and a bigger capacitive arc at the middle-low frequency. The diameters of the two capacitive arcs decreased with exposure times, suggesting the gradual failure of the hybrid material coatings. For quantitative estimate the evolution of the anticorrosion properties of the hybrid material, EIS data were fitted with equivalent circuit, as shown in Fig. 11 and the fitted parameters were listed in Table 2. In the equivalent circuit,  $R_s$  is the solution resistance. As the coating may exhibit heterogeneous nature due to the presence of pores and the failure of coating, the constant phase element  $Q$  in the equivalent circuit was used to represent capacitance.  $Q$  is expressed as  $\omega^{-n}/Y_0(\cos n\pi/2 + j \sin n\pi/2)$ , where  $Y_0$  and  $n$  are the constant and exponent, respectively,  $\omega$  is the angular frequency.<sup>40</sup>  $R_c$  and  $Q_c$  represent the coating resistance and coating capacitance, respectively.  $R_{ct}$  and  $Q_{dl}$  represent the charge-transfer resistance and double-layer capacitance, respectively. Fig. 12 showed the time dependence of  $R_c$  and  $R_{ct}$  of the hybrid material coatings in 3.5% NaCl solution.  $R_c$  represents the physical barrier properties of the coating while the  $R_{ct}$  is determined by the Faradaic process of charge transfer process.<sup>41</sup> It is rather remarkable that both the  $R_c$  and  $R_{ct}$  of the hybrid material-coated electrodes were found to be much higher than those of pure silica. The change of  $Q_{dl}$  is attributed to change of real area of the corroded electrode during the corrosion process.<sup>42</sup> And the  $Q_c$  values of the hybrid material coatings were ranged from  $0.012$  to  $0.021 \mu\text{F cm}^{-2} \text{ Hz}^{1-n_1}$  (10 wt% TESPAT-TEMS), and  $0.0159$  to  $0.0261 \mu\text{F cm}^{-2} \text{ Hz}^{1-n_1}$  (5 wt% TESPAT-TEMS), respectively, which were much lower than that of pure silica coating during the same exposure times. In a word, both the polarization curves and EIS results clearly demonstrated that the hybrid

Table 2 Fitting parameters for the electrical equivalent circuit in Fig. 11

TESPAT content	Time h	$R_s \Omega \text{ cm}^2$	$Q_c \mu\text{F cm}^{-2} \text{ Hz}^{1-n_1}$	$n_1$	$R_c \Omega \text{ cm}^2$	$Q_{dl} \mu\text{F cm}^{-2} \text{ Hz}^{1-n_2}$	$n_2$	$R_{ct} \text{ K}\Omega \text{ cm}^2$
0%	2	0.01	21.9	0.48	210.9	67.7	0.65	3.06
	8	0.01	34.2	0.52	55.1	251	0.55	2.91
	24	0.01	139	0.65	20.1	756	0.63	1.63
2%	2	0.01	0.028	0.83	3856	7.37	0.48	163
	8	0.01	0.435	0.45	2410	15.7	0.46	152
	24	0.01	0.783	1.00	1440	75.6	0.28	36.2
5%	2	0.01	0.0159	0.99	5059	1.56	0.49	279
	8	0.01	0.0258	1.00	4126	2.36	0.47	184
	24	0.01	0.0261	1.00	1532	18.3	0.34	46.6
10%	2	0.01	0.0122	0.96	3031	0.438	0.55	1671
	8	0.01	0.0347	0.56	2301	1.92	0.57	812
	24	0.01	0.0218	1.00	660	8.35	0.54	149



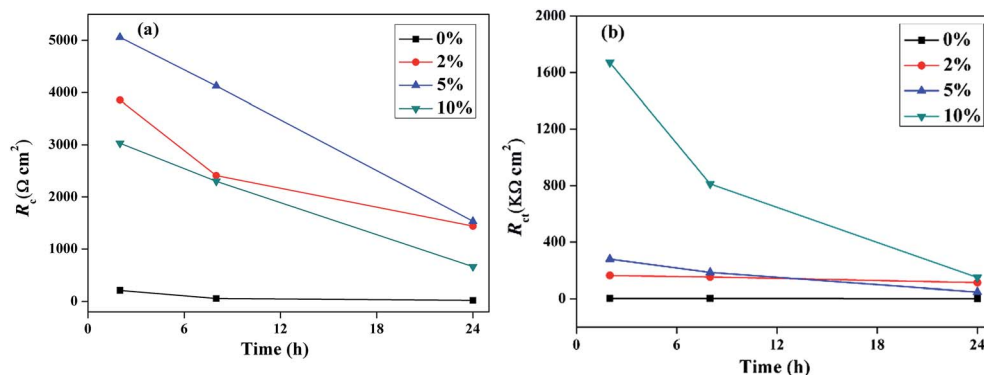


Fig. 12 Time dependence of the coating resistance (a) and charge transfer resistance (b) of the hybrid materials from TESPAT-TEMS at different percentage of TESPAT (0–5 wt%) coated Q235 electrodes exposed to 3.5% NaCl solution.

materials protect the Q235 steel against corrosion better than the pure silica coating does.

It should be noted that the  $R_c$  values of 5 wt% TESPAT-TEMS coating were higher than other coatings during the whole immersion times, suggesting its good film forming property and better barrier property. However, the  $R_{ct}$  values of 10 wt% TESPAT-TEMS coating exhibit better protective effect, because more TESPAT improved the passivation performance on metal matrix,<sup>35</sup> but excessive TESPAT may affect the film forming property of hybrid coating (its  $R_c$  decreased rapidly from 3031 to 660  $\Omega \text{ cm}^2$  with the increase of immersing time). Moreover, the  $i_{\text{corr}}$  values of 5 wt% TESPAT-TEMS ( $1.32 \mu\text{A cm}^{-2}$ ) was much lower than that of 10 wt% TESPAT-TEMS ( $3.89 \mu\text{A cm}^{-2}$ ), and the  $E_{\text{corr}}$  of 5 wt% TESPAT-TEMS ( $-0.557 \text{ V}$ ) was found to be more positive than that of 10 wt% TESPAT-TEMS ( $-0.646 \text{ V}$ ), as shown in Table 1. These results mentioned above indicated that hybrid materials containing 5 wt% TESPAT exhibited better anticorrosion performance based on carbon steel.

## 4. Conclusions

We have synthesized a novel electroactive silsesquioxane precursor, *N*-(3-triethoxysilylpropylureido) aniline tetramer (TESPAT) *via* one-step coupling reaction between aniline tetramer and TESPIC. UV-vis spectra and cyclic voltammetry confirmed the unique electroactivity of TESPAT. Furthermore, new electroactive siliceous hybrid materials have also been successfully prepared through the sol-gel reactions of TESPAT with TEMS at various compositions. The hybrid material exhibits remarkably enhanced corrosion protection as its protection efficiency is better than that of pure silica by a factor of 2.4, based on potentiodynamic polarization measurements performed under saline condition. The significantly improved anticorrosion performance is attributed to the redox catalytic capabilities of the AT units in the hybrid materials.

## Acknowledgements

The research is financially supported by the National Natural Science Foundation of China (Grant no. 21404112) and China Postdoctoral Science Foundation (Grant no. 2014M561798). The

authors thank Dr Qing-Yun Wu in Ningbo University for her suggestion and discussion.

## References

- 1 C. Sanchez, B. Lebeau, F. Chaput and J. P. Boilot, *Adv. Mater.*, 2003, **15**, 1969–1994.
- 2 A. Walcarius, *Chem. Mater.*, 2001, **13**, 3351–3372.
- 3 J. J. E. Moreau and M. W. C. Man, *Coord. Chem. Rev.*, 1998, **178–180**(Part 2), 1073–1084.
- 4 M. R. Detty, R. Ciriminna, F. V. Bright and M. Pagliaro, *Acc. Chem. Res.*, 2014, **47**, 678–687.
- 5 D. Wang and G. P. Bierwagen, *Prog. Org. Coat.*, 2009, **64**, 327–338.
- 6 A. Walcarius, D. Mandler, J. A. Cox, M. Collinson and O. Lev, *J. Mater. Chem.*, 2005, **15**, 3663–3689.
- 7 M. L. Zheludkevich, I. M. Salvado and M. G. S. Ferreira, *J. Mater. Chem.*, 2005, **15**, 5099–5111.
- 8 S. V. Lamaka, M. F. Montemor, A. F. Galio, M. L. Zheludkevich, C. Trindade, L. F. Dick and M. G. S. Ferreira, *Electrochim. Acta*, 2008, **53**, 4773–4783.
- 9 P. Deshpande, N. Jadhav, V. Gelling and D. Sazou, *J. Coat. Technol. Res.*, 2014, **11**, 473–494.
- 10 H. Bhandari, S. A. Kumar and S. K. Dhawan, *Conducting Polymer Nanocomposites for Anticorrosive and Antistatic Applications*, 2012.
- 11 S. P. Zhou, H. M. Zhang, Q. Zhao, X. H. Wang, J. Li and F. S. Wang, *Carbon*, 2013, **52**, 440–450.
- 12 Q. Lu, Q. Zhao, H. M. Zhang, J. Li, X. H. Wang and F. S. Wang, *ACS Macro Lett.*, 2013, **2**, 92–95.
- 13 Y. Kim, K. Teshima and N. Kobayashi, *Electrochim. Acta*, 2000, **45**, 1549–1553.
- 14 K. Brazdžiuvienė, I. Jurevičiūtė and A. Malinauskas, *Electrochim. Acta*, 2007, **53**, 785–791.
- 15 Y. Chen, X. H. Wang, J. Li, J. L. Lu and F. S. Wang, *Electrochim. Acta*, 2007, **52**, 5392–5399.
- 16 Y. P. Li, H. M. Zhang, X. H. Wang, J. Li and F. S. Wang, *Corros. Sci.*, 2011, **53**, 4044–4049.
- 17 T. I. Yang, C. W. Peng, Y. L. Lin, C. J. Weng, G. Edgington, A. Mylonakis, T. C. Huang, C. H. Hsu, J. M. Yeh and Y. Wei, *J. Mater. Chem.*, 2012, **22**, 15845–15852.

- 18 F. Chen and P. Liu, *ACS Appl. Mater. Interfaces*, 2011, **3**, 2694–2702.
- 19 K.-Y. Huang, Y.-S. Jhuo, P.-S. Wu, C.-H. Lin, Y.-H. Yu and J.-M. Yeh, *Eur. Polym. J.*, 2009, **45**, 485–493.
- 20 H. Y. Huang, T. C. Huang, T. C. Yeh, C. Y. Tsai, C. L. Lai, M. H. Tsai, J. M. Yeh and Y. C. Chou, *Polymer*, 2011, **52**, 2391–2400.
- 21 S.-C. Lin, C.-S. Wu, J.-M. Yeh and Y.-L. Liu, *Polym. Chem.*, 2014, **5**, 4235.
- 22 K. C. Chang, H. I. Lu, C. W. Peng, M. C. Lai, S. C. Hsu, M. H. Hsu, Y. K. Tsai, C. H. Chang, W. I. Hung, Y. Wei and J. M. Yeh, *ACS Appl. Mater. Interfaces*, 2013, **5**, 1460–1467.
- 23 C.-J. Weng, C.-H. Chang, C.-W. Peng, S.-W. Chen, J.-M. Yeh, C.-L. Hsu and Y. Wei, *Chem. Mater.*, 2011, **23**, 2075–2083.
- 24 Z. C. Sun, L. Kuang, X. B. Jing, X. H. Wang, J. Li and F. S. Wang, *Chem. Res. Chin. Univ.*, 2002, **23**, 496–499.
- 25 H. Wang, P. Guo and Y. Han, *Macromol. Rapid Commun.*, 2006, **27**, 63–68.
- 26 Z. Yang, X. Wang, Y. Yang, Y. Liao, Y. Wei and X. Xie, *Langmuir*, 2010, **26**, 9386–9392.
- 27 L. Chen, Y. Yu, H. Mao, X. Lu, W. Zhang and Y. Wei, *Mater. Lett.*, 2005, **59**, 2446–2450.
- 28 Y. Guo, A. Mylonakis, Z. T. Zhang, P. I. Lekes, K. Levon, S. X. Li, Q. W. Feng and Y. Wei, *Macromolecules*, 2007, **40**, 2721–2729.
- 29 H. Cui, Y. Liu, Y. Cheng, Z. Zhang, P. Zhang, X. Chen and Y. Wei, *Biomacromolecules*, 2014, **15**, 1115–1123.
- 30 Y. Wu, B. Guo and P. X. Ma, *ACS Macro Lett.*, 2014, **3**, 1145–1150.
- 31 F. Rubio, J. Rubio and J. L. Oteo, *Spectrosc. Lett.*, 1998, **31**, 199–219.
- 32 R. Chen and B. C. Benicewicz, *Macromolecules*, 2003, **36**, 6333–6339.
- 33 D. W. DeBerry, *Journal of The Electrochemical Society*, 1985, **132**, 1022–1026.
- 34 Y. Wei, C. C. Yang, T. Z. Ding, J. M. Yeh and G. Wei, *Abstracts of Papers of the American Chemical Society*, 1996, 211, p. 128-PMSE.
- 35 H. Y. Huang, T. C. Huang, J. C. Lin, J. H. Chang, Y. T. Lee and J. M. Yeh, *Mater. Chem. Phys.*, 2013, **137**, 772–780.
- 36 J. L. Lu, N. J. Liu, X. H. Wang, J. Li, X. B. Jing and F. S. Wang, *Synth. Met.*, 2003, **135**, 237–238.
- 37 T. C. Huang, Y. A. Su, T. C. Yeh, H. Y. Huang, C. P. Wu, K. Y. Huang, Y. C. Chou, J. M. Yeh and Y. Wei, *Electrochim. Acta*, 2011, **56**, 6142–6149.
- 38 K.-Y. Huang, C.-L. Shiu, P.-S. Wu, Y. Wei, J.-M. Yeh and W.-T. Li, *Electrochim. Acta*, 2009, **54**, 5400–5407.
- 39 T. T. X. Hang, T. A. Truc, N. T. Duong, N. Pébère and M.-G. Olivier, *Prog. Org. Coat.*, 2012, **74**, 343–348.
- 40 S. Liu, H. Sun, L. Sun and H. Fan, *Corros. Sci.*, 2012, **65**, 520–527.
- 41 H. Huang, X. Guo, G. Zhang and Z. Dong, *Corros. Sci.*, 2011, **53**, 1700–1707.
- 42 H. Huang, X. Guo, G. Zhang and Z. Dong, *Corros. Sci.*, 2011, **53**, 3446–3449.